



# Formation of a Solar Filament by Magnetic Reconnection, Associated Chromospheric Evaporation, and Subsequent Coronal Condensation

Bo Yang<sup>1,2,3</sup> , Jiayan Yang<sup>1,2</sup> , Yi Bi<sup>1,2</sup> , Junchao Hong<sup>1,2</sup> , and Zhe Xu<sup>4</sup>

<sup>1</sup> Yunnan Observatories, Chinese Academy of Sciences, 396 Yangfangwang, Guandu District, Kunming, 650216, People's Republic of China; [boyang@ynao.ac.cn](mailto:boyang@ynao.ac.cn)

<sup>2</sup> Center for Astronomical Mega-Science, Chinese Academy of Sciences, 20A Datun Road, Chaoyang District, Beijing, 100012, People's Republic of China

<sup>3</sup> Key Laboratory of Solar Activity, National Astronomical Observatories of Chinese Academy of Science, Beijing, 100012, People's Republic of China

<sup>4</sup> Purple Mountain Observatory, Chinese Academy of Sciences, No. 8 Yuanhua Road, Qixia District, Nanjing 210034, People's Republic of China

Received 2021 September 9; revised 2021 October 20; accepted 2021 October 20; published 2021 November 5

## Abstract

We present the first observation of a solar filament formed by magnetic reconnection, associated chromospheric evaporation, and subsequent coronal condensation. Driven by shearing motion during flux emergence, a sequential tether-cutting reconnection process occurred and resulted in an M1.3 confined flare accompanied by the formation of a sigmoid structure. It is found that the flare had conjugate compact footpoint brightenings, which correspond to the footpoints of the sigmoid. Furthermore, observational evidence of explosive evaporation is well diagnosed at the conjugate footpoint brightenings in the impulsive phase of the flare. After the flare, continuous cool condensations formed at about the middle section of the sigmoid and then moved in opposite directions along the sigmoid, eventually leading to the formation of the filament. These observations suggest that magnetic reconnection can not only form the magnetic field structure of the filament but also heat the chromospheric footpoints during their formation and drive chromospheric evaporation. As a result, the heated chromospheric plasma may be evaporated into the magnetic field structure of the filament, where the accumulated hot plasma might suffer from thermal instability or nonequilibrium, causing catastrophic cooling and coronal condensation to form the cool, dense material of the filament. This observation lends strong support to the evaporation–condensation model and highlights the crucial role of magnetic reconnection in forming both the magnetic field structure and the cool, dense material of the filaments.

*Unified Astronomy Thesaurus concepts:* [Solar filaments \(1495\)](#); [Solar prominences \(1519\)](#); [Solar activity \(1475\)](#); [Solar flares \(1496\)](#); [Solar magnetic fields \(1503\)](#); [Solar magnetic reconnection \(1504\)](#); [Solar magnetic flux emergence \(2000\)](#)

*Supporting material:* animations

## 1. Introduction

Solar filaments are filled with cool, dense plasma, manifesting as cool clouds suspended in the surrounding hot tenuous corona. They appear as elongated absorption features on the solar disk in  $H_{\alpha}$  and some extreme ultraviolet (EUV) lines (Anzer & Heinzel 2005). Outside the solar disk, they appear as emitting plasma structures called “prominences.” Filaments are usually formed above the polarity inversion lines (PILs), which separate positive and negative magnetic flux regions in the photosphere (Martin 1998). It has become a consensus that the magnetic field supports the cold and dense plasma of filaments against gravity in the corona. Despite over a century of increasingly detailed observations and studies, the mechanism accounting for filament formation is still controversial. Unraveling the mechanism of filament formation requires a thorough understanding of the formation of the magnetic structure and the cool, dense plasma of filaments.

As stressed by Chen et al. (2020b), a filament should be a coronal structure. Many direct measurements of prominence magnetic fields have shed some light on the magnetic structure of prominences (Leroy 1989; Orozco Suárez et al. 2014; Schmieder et al. 2014). However, it is difficult to determine prominence magnetic fields due to the ambiguity of Stokes inversion or the coronal magnetic fields surrounding the prominences. The detailed

magnetic structure of filaments is still far from being fully understood. Nevertheless, previous theoretical and observational studies of filaments have deepened our understanding of the magnetic structure of filaments. Sheared arcades (Kippenhahn & Schlüter 1957; DeVore & Antiochos 2000) and flux ropes (Kuperus & Raadu 1974; van Ballegoijen & Martens 1989) are believed to be suitable for supporting filaments. A flux rope naturally contains magnetic dips above the PILs, and the cool, dense plasma of the filaments is preferentially supported in the dips. A sheared arcade can contain or not contain magnetic dips. Considering a filament is a dynamic entity, Karpen et al. (2001) suggested that filaments can even be supported by sheared arcades without magnetic dips. Both sheared arcades and flux ropes can be formed by the surface or subsurface mechanisms (see the review by Mackay et al. 2010). In the surface mechanisms (van Ballegoijen & Martens 1989; Martens & Zwaan 2001), magnetic reconnection occurs between a series of magnetic arcades straddling the PILs to form the sheared arcades or flux ropes, under the joint action of photospheric shear flows parallel to the PILs and converging flows perpendicular to the PILs. In the subsurface mechanisms, a preexisting flux rope in the convection zone partly emerges through the solar surface into the corona by buoyancy (Rust & Kumar 1994; Fan 2001). Hitherto, a great deal of observations have tended to support the surface mechanisms (Chae et al. 2001; Yang et al. 2015, 2016; Yan et al. 2016; Yang & Chen 2019; Chen et al. 2020a), and only a handful of observations have been in favor of the subsurface mechanisms (Okamoto et al. 2008; Lites et al. 2010; Xu et al. 2012; Yan et al. 2017).



Original content from this work may be used under the terms of the [Creative Commons Attribution 4.0 licence](#). Any further distribution of this work must maintain attribution to the author(s) and the title of the work, journal citation and DOI.

It is generally accepted that the filament plasma originates from the solar chromosphere (Song et al. 2017; Chen et al. 2020b), but the mechanism by which the chromospheric plasma is transported into the corona to form filaments is still under debate. Historically, there are three promising models for chromospheric plasma being transported into the corona to form filaments (Mackay et al. 2010; Chen et al. 2020b). The first is the injection model, which demonstrated that chromospheric plasma can be injected into a filament channel through magnetic reconnection (Wang 1999; Liu et al. 2005; Wang et al. 2018; Shen et al. 2019; Yang et al. 2019; Wei et al. 2020). The second is the levitation model, which suggested that chromospheric plasma can be directly lifted to the corona by emerging flux or magnetic flux cancellation (Rust & Kumar 1994; Zhao et al. 2017). The third is the evaporation–condensation model, which proposed that chromospheric plasma can be heated to several million kelvin and evaporated into the corona, and then thermal instability (Parker 1953; Field 1965) or thermal nonequilibrium (Antiochos & Klimchuk 1991; Antiochos et al. 2000) causes catastrophic cooling and coronal condensation. The essence of this model is that artificial localized heating concentrated exclusively at the chromospheric footpoints of magnetic loops is needed to heat the chromosphere and then drive chromospheric evaporation. More recently, Huang et al. (2021) tried to unify the injection and evaporation–condensation models in a single framework. They found that when the localized heating is situated in the upper chromosphere, the local plasma is heated to evaporate into the corona; when the localized heating is situated in the lower chromosphere, the enhanced gas pressure pushes the cold upper chromospheric material to be injected into the corona. On the basis of the evaporation–condensation model, an increasing number of numerical simulations have successfully simulated the formation of filaments with steady or nonsteady localized heating symmetrically or asymmetrically distributed at the two chromospheric ends of the filaments (Karpen & Antiochos 2008; Xia et al. 2011; Luna et al. 2012; Keppens & Xia 2014; Xia & Keppens 2016; Zhou et al. 2020). Moreover, many dynamic phenomena of filaments, such as filament oscillations (see the review by Chen et al. 2020b), moving blobs (Luna et al. 2012; Xia & Keppens 2016), plasma circulation of long-lived filaments (Xia & Keppens 2016), cold  $H_\alpha$  counterstreaming flows (Xia et al. 2011; Zhou et al. 2020), and hot EUV counterstreaming flows between filament threads (Zhou et al. 2020), have also been simulated.

The evaporation–condensation model has been extensively and thoroughly analyzed in numerical simulations, but complete and definitive observations that support and validate this model have not yet been reported. So far, only two undisputed observations of coronal condensation forming prominences have been reported. Liu et al. (2012) presented a clear observation that coronal condensation occurs at the magnetic dips of a transequatorial loop system and results in the formation of a cloud prominence after a confined eruption. Soon after, Berger et al. (2012) observed the dynamic formation of a quiescent polar crown prominence in a coronal cavity and implied that the prominence is formed via in situ condensation of hot plasma from the coronal cavity. In both cases, it is not clear whether the hot plasmas originate from chromospheric evaporation. The direct injection (Wang et al. 2007) and even magnetothermal convection involving emerging magnetic bubbles and plumes (Berger et al. 2011) are potential sources of the hot plasmas. In addition,

recent numerical simulation (Kaneko & Yokoyama 2017) and observations (Li et al. 2018, 2021) also proposed that apart from artificial localized heating in the chromosphere, magnetic reconnection in the corona can also trigger thermal instability and result in coronal condensation. In this paper, we report the first definitive observation that magnetic reconnection and associated chromospheric evaporation followed by coronal condensation lead to the formation of a filament. This observation may enhance our understanding of the filament formation.

## 2. Observations

The event was well observed by the Atmospheric Imaging Assembly (AIA; Lemen et al. 2012) and the Helioseismic and Magnetic Imager (HMI; Schou et al. 2012) on board the Solar Dynamics Observatory (SDO; Pesnell et al. 2012). The AIA takes the full-disk images of the Sun in seven EUV and two ultraviolet (UV) wavelengths with a pixel size of  $0''.6$  at a high cadence of up to 12 s. Here the level 1.5 images centered at 304 Å (He II, 0.05 MK), 171 Å (Fe IX, 0.6 MK), 193 Å (Fe XII, 1.3 MK and Fe XXIV, 20 MK), 211 Å (Fe XIV, 2 MK), 335 Å (Fe XVI, 2.5 MK), 94 Å (Fe XVIII, 7 MK), 131 Å (Fe VIII, 0.6 MK and Fe XXI, 10 MK), and 1600 Å (C IV + cont., 0.01 MK) were adopted to study the event. The HMI provides full-disk continuum intensity images and vector magnetic field data with a pixel size of  $0''.5$ . The time cadences of the HMI are 45 s (for the continuum intensity images) and 720 s (for vector magnetic field data). In addition, we used  $H_\alpha$  images from the Global Oscillation Network Group (GONG) and the New Vacuum Solar Telescope (NVST; Liu et al. 2014), the soft X-ray (SXR) flux of the flare at 1–8 Å from the Geostationary Operational Environmental Satellites (GOES), and an SXR image from the X-ray Telescope (XRT; Golub et al. 2007) on board the Hinode (Kosugi et al. 2007) satellite. Images taken from the AIA, HMI, and GONG were aligned by differentially rotating to the reference time of 22:30 UT on 2014 February 2.

To detect the chromospheric evaporation, the spectroscopic data from the EUV Imaging Spectrometer (EIS; Culhane et al. 2007) on board Hinode were also analyzed. We mainly used the EIS data during the period of 21:31:12 UT and 21:39:58 UT that corresponds to the impulsive phase of the flare. The EIS observed this flare with 15 spectral windows using a  $2''$  wide slit and  $3''$  step size with an exposure time of 5 s. The spectra were taken at 80 positions, and it took an average duration of 8 minutes to scan an area of  $240'' \times 304''$ . Here we concentrated on three strong emission lines, He II 256.32, Fe XV 284.16, and Fe XVI 262.98 Å, which provide temperature coverage from the chromosphere ( $\log T \approx 4.7$ ) to the corona ( $\log T \approx 6.4$ ). The EIS level 0 data were performed with the standard Solar Software (SSW) `eis_prep.pro` routine to correct the dark current, detector bias, hot pixels, cosmic rays, and radiometric calibration. Meanwhile, the orbital variation and wavelength calibration were also corrected by using housekeeping data (Kamio et al. 2010). Then, we used the standard SSW `eis_auto_fit.pro` routine with a single Gaussian model to derive spectral intensities, line widths, and Doppler velocities. To derive the reference wavelengths of the three strong emission lines, the average line centers of the He II, Fe XV, and Fe XVI lines for the quieter region of the EIS field of view (FOV) were measured. The Doppler velocities estimated by the Doppler shift in these emission lines have a few kilometers per second uncertainty.

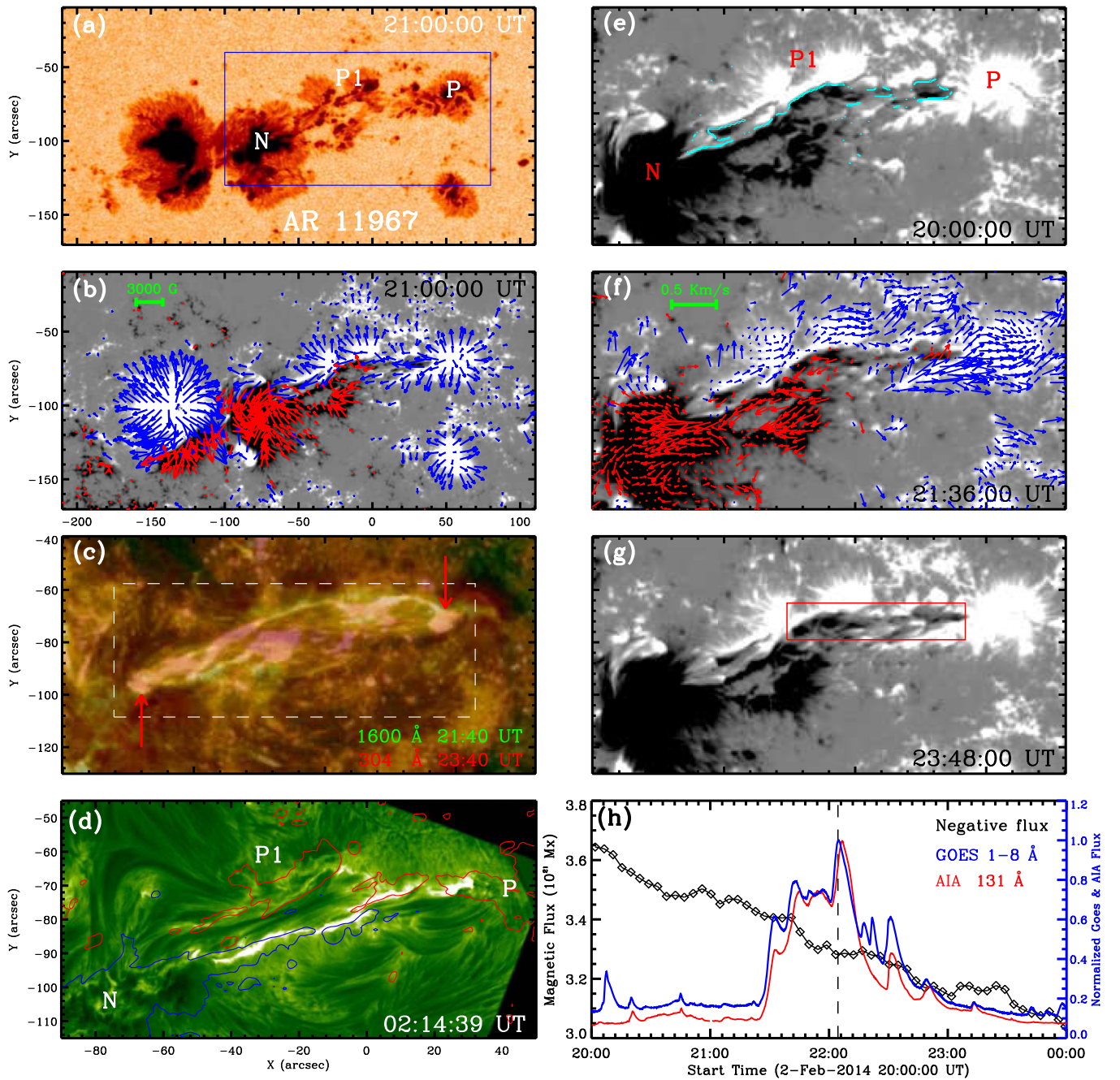


**Figure 1.** (a) and (b) Continuum intensity image and vector magnetogram of AR 11967 taken by SDO/HMI at 21:00 UT on 2014 February 2. (c) Composite image of the AIA 1600 and 304 Å passbands displaying the ribbons for the M1.3 flare and the formed filament. The two red arrows point to the conjugate compact footpoint brightenings of the flare. (d) NVST  $H_{\alpha}$  image, along with HMI vertical magnetic field contours overplotted as red/blue at  $\pm 800$  G levels. (e)–(g) Vertical component of the HMI vector magnetic field showing the cancellation of opposite polarities in the core region of the flare. The cyan curves outline the main PILs. The red (blue) arrows are the horizontal magnetic field vectors in panel (b) and the tangential velocity vectors in panel (f), which originate from negative (positive) longitudinal fields. The tangential velocity vectors are inferred from the DAVE4VM technique and averaged from 20:00 UT to 22:00 UT. Labels “P” and “P1” register the sunspots with positive polarity, while “N” denotes the sunspot with negative polarity. (h) Normalized GOES SXR flux at 1–8 Å, normalized AIA 131 Å light curves extracted from the dashed rectangle, and unsigned negative magnetic flux averaged over the red rectangle. The vertical dashed line marks the peak time of the flare. The blue rectangle denotes the FOV of panels (c) and (e)–(g).

### 3. Results

#### 3.1. Overview of AR 11967 and Photospheric Magnetic Field Evolution

On 2014 February 2, NOAA AR 11967 was located at about  $S13^{\circ}E04^{\circ}$ . Figures 1(a) and (b) illustrate the general appearance of the active region (AR). On this day, four M-class flares occurred in this AR, three of which had unique X-shaped

ribbons and occurred in a facular region of the AR (for a detailed analysis of these flares, see Liu et al. 2016), and one had the typical two ribbons and took place in the central and northwestern sections of the AR (enclosed by the blue box in Figure 1(a)). Here we focus on the M1.3 two-ribbon flare, which started at about 21:24 UT, peaked at 22:04 UT, and ended at 22:14 UT in GOES 1–8 Å flux. Apart from its two ribbons, the most striking feature of this flare is that it had

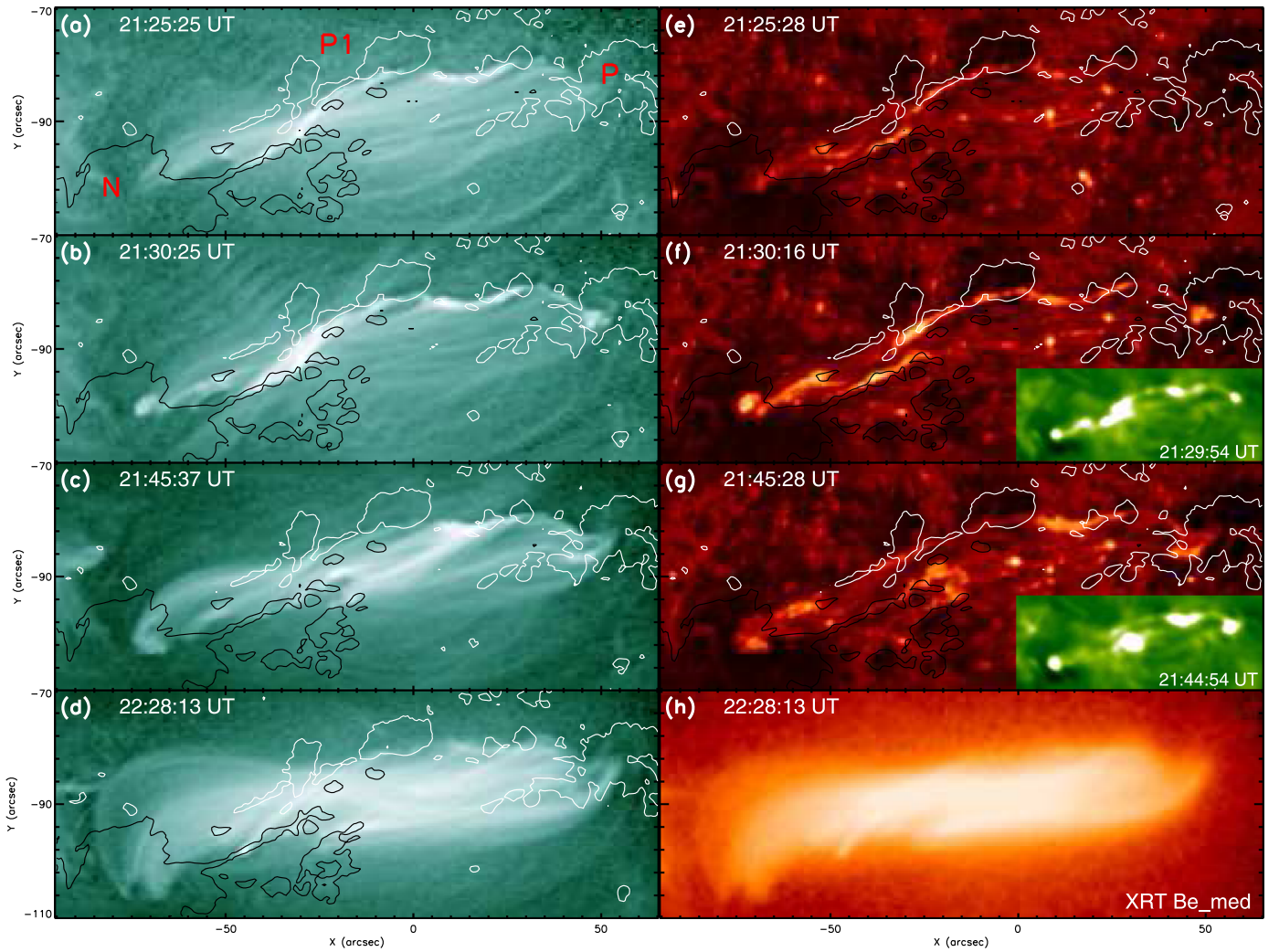


**Figure 2.** The SDO/AIA 94 Å (panels (a)–(d)) and Hinode/XRT Be-med (panel (h)) images showing the formation of a sigmoid structure and AIA 1600 Å (panels (e)–(g)) and GONG  $H_{\alpha}$  (insets) images displaying the evolution of the flare ribbons. Iso-Gauss contours of  $\pm 800$  G are superposed by white and black curves in panels (a)–(g). An animation of panels (a)–(d) and (e)–(g) is available. The animation spans from 21:00:37 UT to 22:39:52 UT on 2014 February 2, and the time cadence is 9 s.

(An animation of this figure is available.)

conjugate compact footpoint brightenings (Figure 1(c)). The conjugate compact footpoint brightenings were more pronounced in the  $H_{\alpha}$  observations (see the inserted images in Figure 2). They were distributed on the sunspots with opposite polarities and corresponded to the footpoints of the subsequent formed filament (Figures 1(c) and (d)).

The central and northwestern sections of the AR, where the flare of interest occurred, developed rapidly and formed a contiguous penumbral structure (Figure 1(a)) due to magnetic flux emergence. The emerging magnetic flux was characterized by one negative sunspot, labeled “N,” and two major positive sunspots, labeled “P” and “P1” (Figure 1(a)). There was constant flux emergence between P and N. A significant flux of positive polarity emerged toward and merged with P, and a significant flux of negative polarity emerged to the east of P and then migrated eastward into N, forming an elongated channel of negative magnetic fluxes (Figure 1(b)). For the sake of description, we call the elongated channel the negative magnetic channel. In this region, the photospheric magnetic field was highly sheared with respect to the PILs (Figure 1(b)). It is notable from the NVST high-resolution  $H_{\alpha}$  image (Figure 1(d)) that the emerged sunspots

with opposite polarities were connected by highly sheared arch filament systems. Figures 1(e)–(g) show the evolution of the photospheric magnetic field before, during, and after the flare, covering part of the episodes of the flux emergence. It is clear that there was significant flux cancellation ongoing along the main PILs of this region. Unsigned negative flux integrated in a red rectangle (Figure 1(g)) is shown in Figure 1(h). This region was selected to avoid the negative magnetic flux that continuously migrated along the negative magnetic channel into N. One can see that the unsigned negative flux persistently decreased from the beginning to the end of the observation. Applying the inductive DAVE4VM (Schuck 2008) method to the 12 minute cadence HMI vector magnetic field data, we calculated the photospheric velocity field, which integrated over 2 hr between 20:00 UT and 22:00 UT and superimposed on an HMI vertical image (Figure 1(f)). Remarkably, persistent northwestward photospheric flows characterize the positive sunspots P and P1, while southeastward photospheric flows dominate the negative sunspot N and the negative magnetic channel, displaying overall strong shearing motion over the core region of the flare. These observations are suggestive that the flux cancellation ongoing

along the PILs may be driven by the strong shearing motion and is tightly related to the triggering of the flare and the subsequent formation of the filament.

### 3.2. The Flare Associated with the Formation of a Sigmoid

The light curves of AIA 131 Å and GOES 1–8 Å SXR flux display multiple impulsive peaks in the course of the flare (Figure 1(h)). This is similar to our previous observations (Yang & Chen 2019) that each impulsive peak may correspond to a magnetic reconnection process. Figures 2(a)–(d) show the evolution of the flare associated with the formation of a sigmoid structure. It is clear that a set of brighter and shorter hot loops, which apparently connect P1 to the negative magnetic channel, first appeared near the negative sunspot N (panels (a) and (b)). Afterward, another set of brighter and shorter hot loops, which connect the positive magnetic flux patches between P and P1 to the negative magnetic channel, appeared close to the positive sunspot P (panel (c)). These hot loops appearing at different locations may be indicative of multiple magnetic reconnection processes occurring at different locations and times. As the flare progressed, longer hot loops apparently rooted in P and N were gradually formed and finally shown as a remarkable sigmoid structure (panels (d) and (h)). The sigmoid formed along the main PILs and had an inverse S-shape, which suggests a negative, left-handed twist.

The evolution of the flare ribbons is shown in Figures 2(e)–(g). The flare ribbons first appeared at the region where the negative magnetic channel was in contact with P1 (panel (e)). These ribbons were distributed on either side of the main PILs and in line with the footpoints of the hot loops that appeared near N (panels (a) and (e)). Then, they developed parallel to the main PILs in opposite directions and formed a two-ribbon flare (panel (f)). It is worth mentioning that conjugate compact footpoint brightenings appeared at P and N (panel (f)) that were consistent with the footpoints of the formed sigmoid (panels (d) and (h)). Subsequently, more intense flare brightenings occurred at the footpoints of the hot loops that appeared close to P (panel (g)). At the same time, the area of the conjugate compact footpoint brightenings was further expanded. It is evident from the inserted  $H_{\alpha}$  images that the most pronounced flare ribbons correspond to the conjugate compact footpoint brightenings and the footpoints of the hot loops. They showed up as four compact footpoint brightenings in the  $H_{\alpha}$  observation at about 21:44:54 UT. This flare was confined, the two main ribbons did not separate perpendicular to the PILs, and there were no clear coronal mass ejection signatures. These observations, taken together with the photospheric observations introduced before, are highly reminiscent of the tether-cutting reconnection scheme (Moore et al. 2001; Liu et al. 2013; Chen et al. 2014, 2018). More precisely, our observations fit very well with the physical picture that a confined flare is triggered by the tether-cutting reconnection process. Therefore, we argue that the confined flares associated with the formation of the sigmoid in the present study are the results of a sequential tether-cutting reconnection process that occurred between the magnetic fields connecting P to the negative magnetic channel and the magnetic fields connecting P1 and its nearby positive flux patches to N. Moreover, these reconnections may be driven by the strong shearing motion during the flux emergence.

### 3.3. Chromospheric Evaporation at the Conjugate Footpoint Brightenings

Chromospheric evaporation, first described by Neupert (1968), refers to the process during a solar flare in which chromospheric materials are heated and then expand rapidly upward into the low-density corona, thus filling up the coronal loops and giving the hot and dense postflare loops that can be visible at the EUV and SXR wavelengths. This process occurs when the flare energy deposited in the chromosphere by nonthermal electrons or thermal conduction exceeds what can be shed by radiative losses. The blueshifts that correspond to plasma upflows in emission lines formed at flare temperatures provide strong evidence for chromospheric evaporation. It is recognized that the evaporation is identified as explosive when emission lines formed at flare temperatures exhibit blueshifts, while emission lines formed at chromospheric and transition region temperatures exhibit redshifts; the evaporation is considered to be gentle when emission lines formed at all temperatures exhibit blueshifts (Fisher et al. 1985; Brosius 2009; Milligan & Dennis 2009; Chen & Ding 2010; Li & Ding 2011; Young et al. 2013; Tian et al. 2015).

Using spectroscopic observations from Hinode/EIS, chromospheric evaporation at the conjugate footpoint brightenings is well diagnosed. Figures 3(a)–(c) show the spatial distribution of line intensity, Doppler velocity, and line width for the Fe XV 284.16 Å line in the impulsive phase of the flare. The conjugate footpoint brightenings are the sites of rapid chromospheric heating; they are also shown as a pair of intense, compact brightenings in the Fe XV 284.16 Å emission line (panel (a)). It is evident from the Doppler velocity map (panel (b)) that the conjugate footpoint brightenings are dominated by blueshifts. In particular, these blueshifts are accompanied by relatively large line widths (panel (c)). We selected two points, which are denoted by crosses and marked “1” and “2,” to extract the He II 256.32, Fe XV 284.16, and Fe XVI 262.98 Å line profiles. Point 1 lies in the positive footpoint of the conjugate footpoint brightenings, while point 2 lies in the negative footpoint of the conjugate footpoint brightenings. The EIS scanned points 1 and 2 at 21:32:47 UT and 21:37:20 UT, respectively. The He II, Fe XV, and Fe XVI line profiles at point 1 are displayed in Figures 3(d)–(f), and those at point 2 are displayed in Figures 3(g)–(i). We fitted all of the line profiles at points 1 and 2 using a single Gaussian function. The fitting results are shown as red curves in Figures 3(d)–(i). It is seen that the chromospheric He II line shows significant redshifts, while the coronal Fe XV and Fe XVI lines show significant blueshifts at both locations. The redshift velocities are measured to be 14.1 and 14.0 km s<sup>-1</sup> at points 1 and 2, respectively. The blueshift velocities are measured to be -28.9 and -11.2 km s<sup>-1</sup> for the Fe XV line and -30.3 and -17.6 km s<sup>-1</sup> for the Fe XVI line at points 1 and 2, respectively. These results reveal that explosive evaporation occurred at the conjugate footpoint brightenings in the impulsive phase of the flare.

### 3.4. Coronal Condensation Resulting in Filament Formation

The explosive evaporation occurring at the conjugate footpoint brightenings may provide heated material to make the formed sigmoid overdense, which is conducive to triggering thermal instability or nonequilibrium, causing catastrophic cooling and coronal condensation. Figure 4 presents the formation and evolution of cool condensations in the sigmoid and the formation

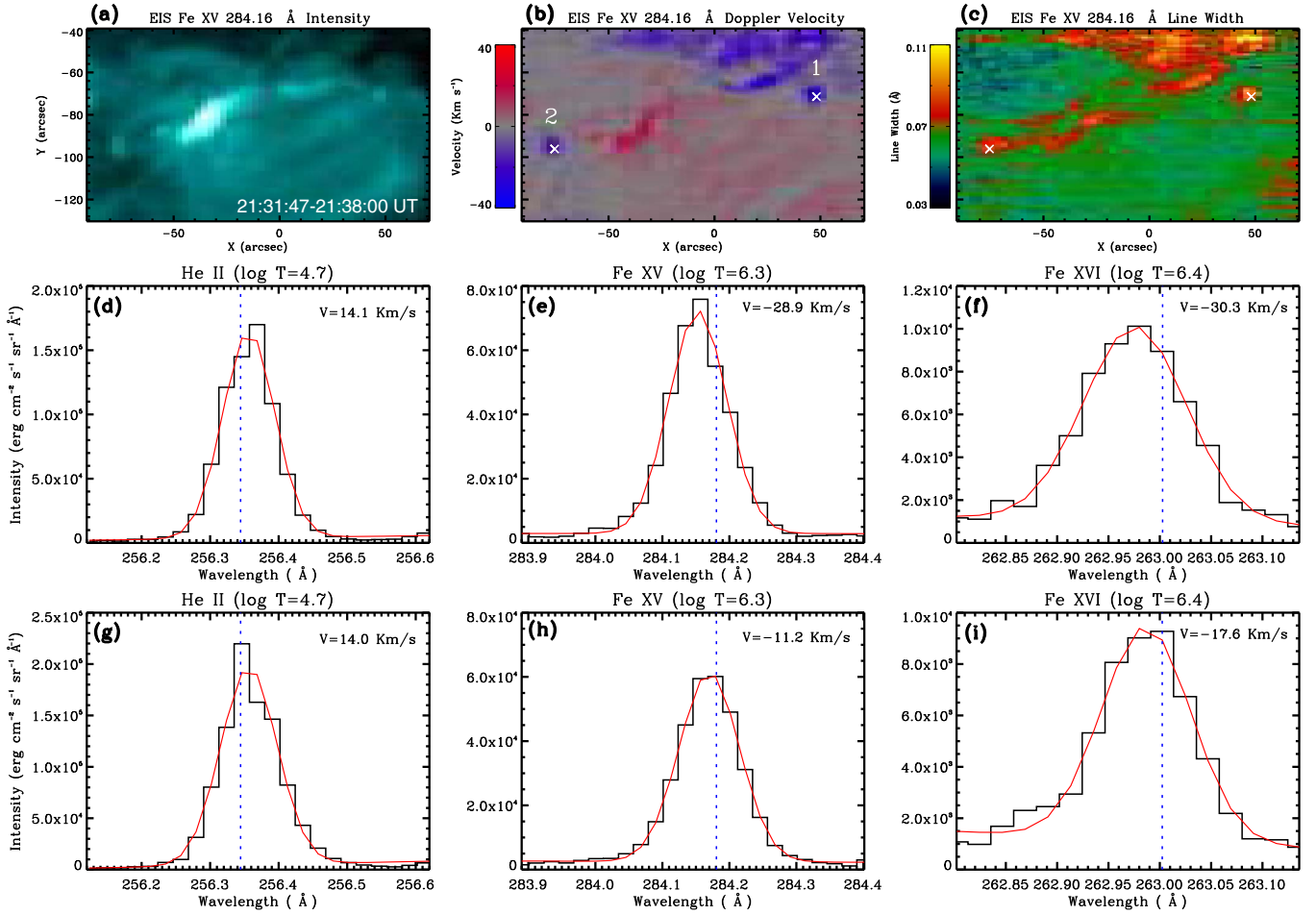


**Figure 3.** (a)–(c) Hinode/EIS Fe XV 284.16 Å intensity, Doppler velocity, and line width maps. The crosses marked “1” and “2” are selected to perform a detailed spectral analysis. Panels (d)–(f) and (g)–(i) are line profiles and fitting results for the He II, Fe XV, and Fe XVI lines at points 1 and 2, respectively. The histograms are observed profiles, and the red curves are fitting results. The dotted lines represent the rest wavelengths as measured from quiet-Sun regions.

of a filament. At 22:50:38 UT, about 34 minutes after the flare ended, a set of bright loops gradually appeared (panel (a1)). At the same time, the initial condensation (as indicated by the red arrow in panel (b1)), which can be clearly identified in the AIA 335 Å observation, formed at about the middle portion of these bright loops. Thereafter, the condensations continued to grow and moved in opposite directions along these bright loops (see panels (a2), (a3), (b2), and (b3) and the associated animation), forming a long filamentary structure (panels (c2) and (c3)). These condensations are short-lived. They finally moved toward and fell rapidly to the footpoints of these bright loops. As a result, the bright loops faded, and the long filamentary structure disappeared. Following the disappearance of the long filamentary structure, another set of bright loops, which has an overall inverse S-shape, gradually appeared (panels (a3) and (a4)). Similarly, the cool condensations first formed at about the middle portion of these inverse S-shaped bright loops; they then continued to grow and moved in opposite directions along these bright loops (panels (a4) and (b4)), resulting in the formation of two long, almost parallel filamentary structures (panel (c4)). As the condensations persistently formed and moved in opposite directions along the two filamentary structures, a filament with an inverse S-shape was formed (panels (a5), (a6), (b5), (b6), (c5), and (c6)). The formed filament was rooted in the locations corresponding to the conjugate footpoint brightenings (see Figure 1(c)), with its positive ends anchored in the positive

sunspot P and its negative ends anchored in the negative sunspot N (panel (c6)). The filament is sinistral, indicating a negative, left-handed twist (Martin 1998), which is in line with the sigmoid.

The gradual emergence of the bright loops should be the result of the gradual cooling of the formed sigmoid over time after the flare. Apparently, the first bright loops that appeared are low-lying relative to the inverse S-shaped bright loops. The successive appearance of cool condensates in the low-lying bright loops and then inverse S-shaped bright loops are consistent with the observation of Liu et al. (2012) and the simulation of Karpen & Antiochos (2008). They implied that cool condensations first formed at those low-lying loops due to their shorter lengths and/or greater densities from gravitational stratification. To trace the dynamic evolution of the cool condensations in the low-lying and inverse S-shaped bright loops, spacetime plots along slices “AB” and “CD” in Figures 4(a1) and (a5) were constructed from AIA 335 Å images, and the result was provided in Figures 5(c) and (d). The cool condensations moved in opposite directions along the low-lying and inverse S-shaped bright loops and are clearly shown on the spacetime plots. We find that the cool condensations moved along the low-lying bright loops to their positive ends with a mean velocity of about 43.3 km s<sup>-1</sup> and their negative ends with a mean velocity of about 39.4 km s<sup>-1</sup>; the cool condensations moved along the inverse S-shaped bright loops to their positive ends with a mean velocity of about

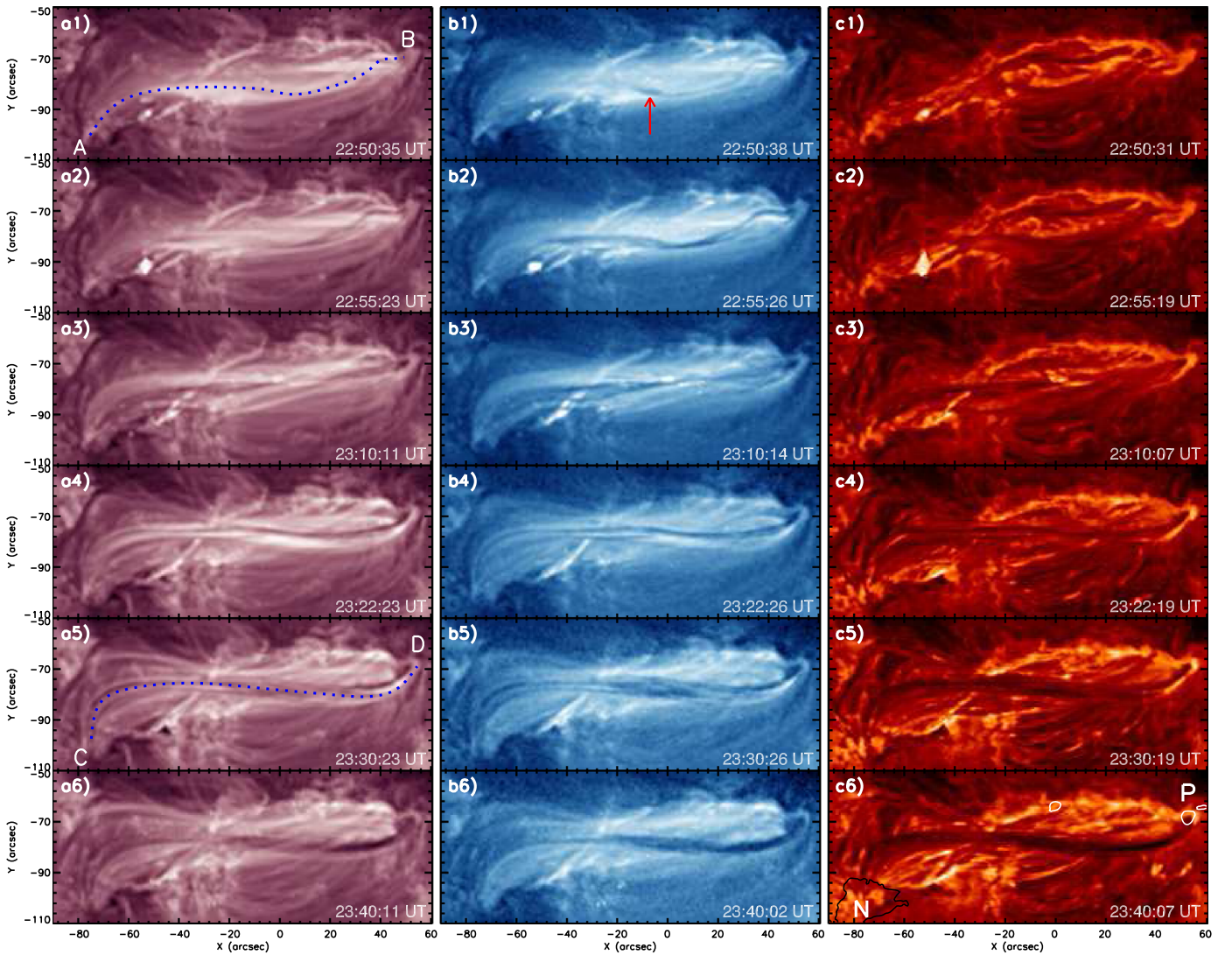


**Figure 4.** Sequence of AIA 211 Å (panels (a1)–(a6)), 335 Å (panels (b1)–(b6)), and 304 Å (panels (c1)–(c6)) images presenting the formation of the filament by coronal condensation. The red arrow points to the location where the initial condensation appeared. The dashed lines “AB” and “CD” mark the slit position of the time slices shown in Figures 5(c) and (d), respectively. Iso-Gauss contours of  $\pm 2000$  G are superposed by white and black curves in panel (c6). An animation including the sequence of AIA 304, 171, 193, 211, 335, 131, and 94 Å images is available. The animation spans from 22:40:01 UT to 23:59:59 UT on 2014 February 2, and the time cadence is 8 s.

(An animation of this figure is available.)

$36.6 \text{ km s}^{-1}$  and their negative ends with a mean velocity of about  $37.1 \text{ km s}^{-1}$ .

As the sigmoid gradually cools over time after the flare, similar to the off-limb condensation events (Berger et al. 2012; Liu et al. 2012; Li et al. 2018), the peak brightness of the appearing bright loops should progressively shift in time from the AIA broadband channels with higher characteristic temperatures to the channels with lower characteristic temperatures. However, this trend cannot be definitively detected in this on-disk observation owing to intermittent magnetic activity that still occurred after the flare. It is interesting to note that a transient brightening (as denoted by the blue arrow in Figure 5(a)) appeared in the inverse S-shaped loops during the formation of the filament. It cooled down over time and finally formed cool condensations (as pointed out by the red arrow in Figure 5(b)) in the inverse S-shaped loops. This transient feature is very similar to the long transient brightening simulated by Luna et al. (2012). They suggested that this long

transient brightening is the consequence of the evaporation and condensation. In the red dashed rectangle enclosing the long transient brightening in Figure 5(a), the light curves of the AIA 211, 193, and 171 Å channels are calculated and displayed in Figure 5(e) as blue, red, and green curves, respectively. It is obvious that the peak brightness of the long transient brightening progressively shifts in time from the 211 Å channel, through the 193 Å channel, to the 171 Å channel. The long transient brightening peaked first in the 211 Å channel at about 23:21:36 UT. With a delay of about 72 s, it peaked in the 193 Å channel at about 23:22:48 UT. Then, it peaked in the 171 Å channel at about 23:23:17 UT, 29 (101) s later than the peak of the AIA 193 (211) Å light curve. These results strongly suggest that hot plasma evaporated from the chromosphere cools down and condenses in the sigmoid to form the cool, dense filament, probably due to the onset of thermal instability or nonequilibrium.

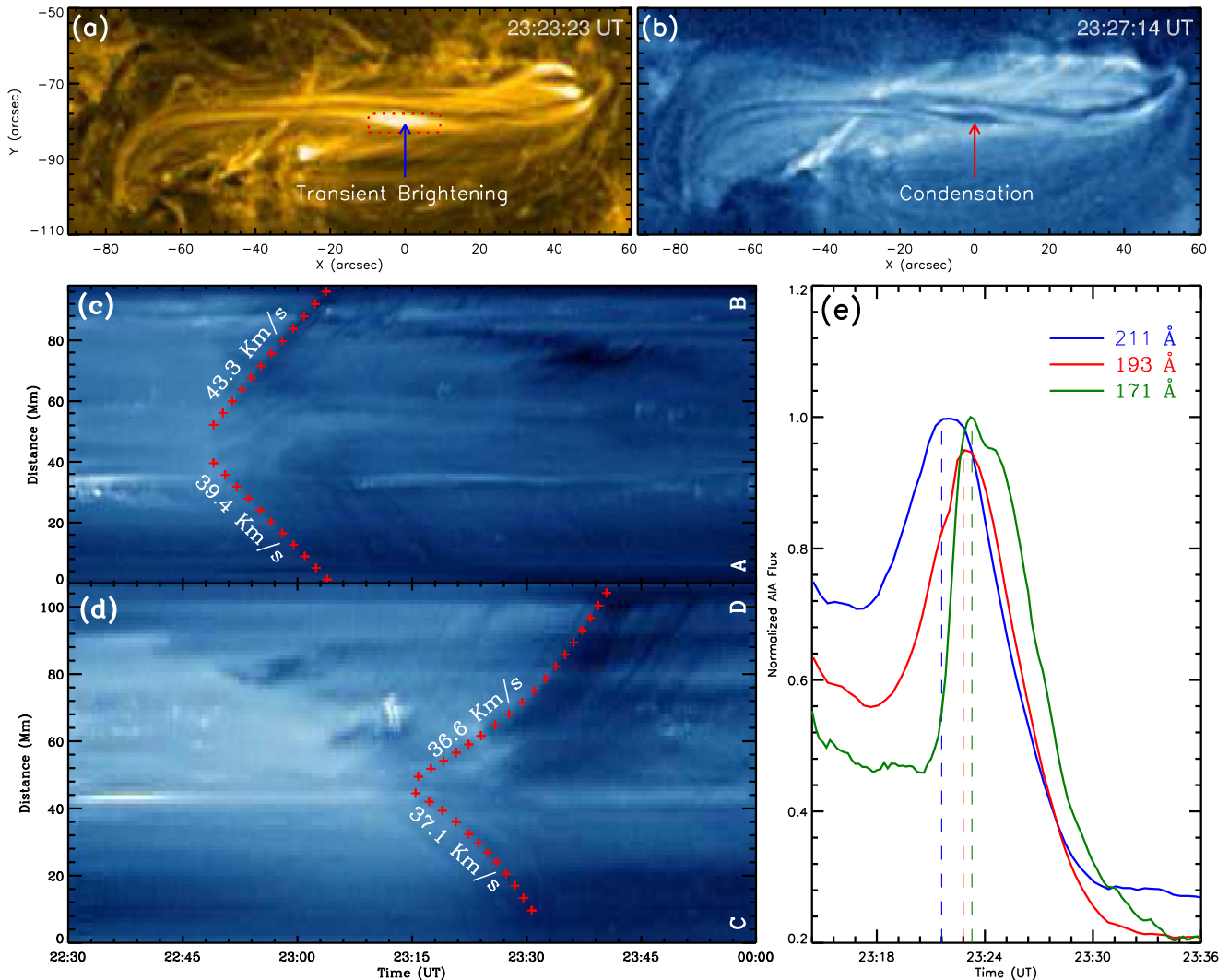


**Figure 5.** The AIA 171 Å (panel (a)) and 335 Å (panel (b)) images show that a long, transient brightening cools to and condenses into the filament over time. (c) and (d) Time-slice plots made from AIA 335 Å images separately along dashed lines AB and CD in Figure 4. The red plus signs outline the motions of the cool condensations. (e) Normalized AIA light curves extracted from the red dashed rectangle.

#### 4. Conclusion and Discussion

In this study, we report a clear observation of a solar filament formed through chromospheric evaporation and subsequent coronal condensation after an M-class confined flare. Our investigations show that this confined flare is triggered by a sequential tether-cutting reconnection process as strong magnetic shear occurring during flux emergence in NOAA AR 11967. Owing to the tether-cutting reconnection, an elongated magnetic structure is newly created above the flaring PIL, which separately bridges its footpoints at two conjugate compact brightening regions. The spectroscopic observations from Hinode/EIS reveal that explosive chromospheric evaporation takes place at the two compact brightening regions in the impulsive phase of the flare. In this course, because of the explosive injection of heated chromospheric plasma from its footpoints, the newborn elongated magnetic structure soon manifests as an X-ray sigmoid. After the flare, cool material continuously condenses in the middle section of the sigmoid and then moves in opposite directions along the magnetic field lines of the sigmoid, eventually resulting in the formation of a filament in the 304 Å passband. This indicates that the evaporated hot plasma, which was trapped in the sigmoid,

cools down to at least  $\sim 0.05$  MK within tens of minutes, possibly due to the onset of thermal instability or nonequilibrium. These observations demonstrate that magnetic reconnection not only directly creates the desirable magnetic field structure for filament formation but also indirectly supplies cold and dense material for the forming filament in tens of minutes through the resultant chromospheric evaporation and subsequent coronal condensation.

Observational evidence of chromospheric evaporation has not been detected in filament formation events, but it has been documented in numerous flare events of different magnitude (Ding et al. 1996; Milligan & Dennis 2009; Ning et al. 2009; Cheng et al. 2015; Li et al. 2015; Zhang et al. 2016; Huang et al. 2020). In the framework of the standard flare model (Priest & Forbes 2002), electrons are accelerated at or near a magnetic reconnection site in the corona, and the accelerated electron beams propagate downward along newly reconnected magnetic field lines and then bombard the chromosphere to generate chromospheric evaporation. Meanwhile, thermal conduction from the reconnection site may also contribute to the heating. In our observation, in the course of the formation of the sigmoid by the sequential tether-cutting reconnection process, it is quite possible that reconnection-accelerated electron beams or thermal conduction from the



reconnection sites may travel or spread along the magnetic field lines of the sigmoid in opposite directions and toward their conjugate chromospheric footpoints. As a result, the conjugate chromospheric footpoints of the sigmoid would be heated, manifesting as the conjugate compact footpoint brightenings. Owing to the heating, as confirmed by the Hinode/EIS spectroscopic observation that explosive evaporation occurred at the conjugate footpoint brightenings, heated chromospheric plasma may thus be evaporated into the sigmoid and make it overdense. Subsequently, thermal instability or nonequilibrium might be triggered, causing catastrophic cooling and coronal condensation to form the cold, dense material of the filament.

The evaporation–condensation model is a promising candidate that accounts for the filament formation. However, unambiguous observations directly validating this model have been missing up to now. A handful of previous observations have shown that coronal condensation can lead to the formation of prominences (Berger et al. 2012; Liu et al. 2012; Viall et al. 2020), but the origin of the hot plasma involved in the coronal condensation has been questionable. In these observations and previous simulations (Antiochos & Klimchuk 1991; Karpen & Antiochos 2008; Luna et al. 2012; Xia & Keppens 2016), the formation of the filament magnetic structure and its cold, dense material have been treated separately. In fact, the formation of filaments is the result of both magnetic and thermal evolution. Kaneko & Yokoyama (2017) proposed a reconnection–condensation model, which treated the formation of the filament magnetic structure and its cool, dense material together, to explain the formation of filaments. It is worth noting that any artificial localized heating in the chromosphere is not considered in their model. Their model does not include the chromosphere, and the resultant prominence mass only reaches the observed lower limit of typical prominence densities. The magnetic reconnection in their model forms the filament magnetic structure and directly triggers thermal instability causing coronal condensation. The reconnection-induced topology changes triggering thermal instability and the formation of cool plasma condensations were subsequently confirmed in coronal rain observations (Li et al. 2018, 2021; Mason et al. 2019). In the present study, the formation of the filament magnetic structure and its cold, dense material are treated together from the perspective of observation for the first time. Our observations demonstrate that the formation of the filament magnetic structures by magnetic reconnection also has a profound influence on the subsequent thermal evolution occurring in it. Different from Kaneko & Yokoyama (2017) and Li et al. (2018), the magnetic reconnection in our observations might affect the subsequent thermal evolution in the filament magnetic structures by heating their chromospheric footpoints during their formation. This is consistent with the evaporation–condensation model (Antiochos & Klimchuk 1991; Antiochos et al. 2000). This observation, for the first time, presents unambiguous observational evidence that both chromospheric evaporation and subsequent coronal condensation take place in the formation of a filament, in support of the evaporation–condensation model.






The formed filament was short-lived. It only lived for about an hour and then gradually disappeared. In the framework of the evaporation–condensation model, numerous simulations have shown that deep magnetic dips are necessary for supporting the cool condensations (Luna et al. 2012; Zhou et al. 2020). In this scenario, a typical dynamic phenomenon that can usually be seen during the filament formation is the longitudinal oscillation of the filament (see the review by Chen et al. 2020b). In the absence of

magnetic dips, the formation of long-lived filaments requires constant chromospheric footpoint heating to maintain a stable cycle, in which plasma evaporates from the chromosphere, condenses into the filament in the corona, and drains back to the chromosphere along the magnetic field lines of the filament (Karpen et al. 2001). In the present study, any oscillations during the formation and disappearance of the filament are not observed. Moreover, continual chromospheric footpoint heating and coronal condensation did not occur after the filament formed. It is likely that the filament might not contain deep magnetic dips, which are suitable for supporting the cool condensations. The cool condensations could not be stably supported in the filament and thus drain in opposite directions along the filament, ultimately causing it to be short-lived. The real and detailed magnetic field structure of the filament needs to be further investigated.

Generally, the formation of a quiescent prominence is days and even weeks long, and the quiescent prominences are long-lived. Berger et al. (2012) found that quiescent prominences can be formed via in situ condensation of hot plasma contained in the core of the coronal cavity. However, the origin of the hot plasma is not yet identified. Although flux emergence and local reconnection have been suggested, the possibility of chromospheric evaporation cannot be ruled out. In the quiet Sun, explosive events, such as reported in this paper, never happen. But during the formation and evolution of the quiescent filaments, photospheric magnetic flux cancellation, which might be closely related to the magnetic reconnection occurring in the lower atmosphere of the Sun, was found to be abundant near the PILs (Martin 1998; Mackay et al. 2010). This process can also heat the footpoints of the reconnected coronal loops (Yang et al. 2016, 2018). It is possible that gentle evaporation might be driven by the magnetic reconnection occurring in the lower atmosphere of the Sun during the formation of the magnetic structure of the quiescent prominences. In addition, Zhou et al. (2020) recently proposed that turbulent heating on the solar surface can randomly evaporate materials from the solar surface to the corona, leading to quiescent prominence formation. So far, observational evidence of chromospheric evaporation has not been observed during the formation and evolution of quiescent prominences. The applicability of the evaporation–condensation model to quiescent prominences needs to be verified by more high-resolution spectral and imaging observations in the future. In the AR, the explosive events reported in this paper could frequently happen, and they are more likely to be associated with AR filament formation.

We thank the referee for valuable suggestions and comments that greatly improved the paper. The authors thank the scientific/engineering team of SDO, Hinode, GOES, NVST, and GONG for providing the excellent data. We would like to thank Dr. Hechao Chen for his fruitful comments. This work is supported by the National Key R&D Program of China (2019YFA0405000); the Natural Science Foundation of China under grants 12073072, 11633008, 11933009, 12173084, 11873088, and 11703084; the CAS “Light of West China” Program; the Open Research Program of the Key Laboratory of Solar Activity of the Chinese Academy of Sciences (KLSA202018); CAS grant “QYZDJ-SSW-SLH012”; the Yunnan Natural Science Foundation under grants 202001AU070052 and 202101AV070004; and the Project Funded by China Postdoctoral Science Foundation 2020M671639.

## ORCID iDs

Bo Yang  <https://orcid.org/0000-0002-1322-9061>  
 Jiayan Yang  <https://orcid.org/0000-0003-3462-4340>  
 Yi Bi  <https://orcid.org/0000-0002-5302-3404>  
 Junchao Hong  <https://orcid.org/0000-0002-3804-7395>  
 Zhe Xu  <https://orcid.org/0000-0002-9121-9686>

## References

- Antiochos, S. K., & Klimchuk, J. A. 1991, *ApJ*, 378, 372  
 Antiochos, S. K., MacNeice, P. J., & Spicer, D. S. 2000, *ApJ*, 536, 494  
 Anzer, U., & Heinzel, P. 2005, *ApJ*, 622, 714  
 Berger, T., Testa, P., Hillier, A., et al. 2011, *Natur*, 472, 197  
 Berger, T. E., Liu, W., & Low, B. C. 2012, *ApJL*, 758, L37  
 Brosius, J. W. 2009, *ApJ*, 701, 1209  
 Chae, J., Wang, H., Qiu, J., et al. 2001, *ApJ*, 560, 476  
 Chen, F., & Ding, M. D. 2010, *ApJ*, 724, 640  
 Chen, H., Duan, Y., Yang, J., et al. 2018, *ApJ*, 869, 78  
 Chen, H., Hong, J., Yang, B., et al. 2020a, *ApJ*, 902, 8  
 Chen, H., Zhang, J., Cheng, X., et al. 2014, *ApJL*, 797, L15  
 Chen, P.-F., Xu, A.-A., & Ding, M.-D. 2020b, *RAA*, 20, 166  
 Cheng, X., Hao, Q., Ding, M. D., et al. 2015, *ApJ*, 809, 46  
 Culhane, J. L., Harra, L. K., James, A. M., et al. 2007, *SoPh*, 243, 19  
 DeVore, C. R., & Antiochos, S. K. 2000, *ApJ*, 539, 954  
 Ding, M. D., Watanabe, T., Shibata, K., et al. 1996, *ApJ*, 458, 391  
 Fan, Y. 2001, *ApJL*, 554, L111  
 Field, G. B. 1965, *ApJ*, 142, 531  
 Fisher, G. H., Canfield, R. C., & McClymont, A. N. 1985, *ApJ*, 289, 425  
 Golub, L., Deluca, E., Austin, G., et al. 2007, *SoPh*, 243, 63  
 Huang, C. J., Guo, J. H., Ni, Y. W., et al. 2021, *ApJL*, 913, L8  
 Huang, Z., Zhang, Q., Xia, L., et al. 2020, *ApJ*, 897, 113  
 Kamio, S., Hara, H., Watanabe, T., et al. 2010, *SoPh*, 266, 209  
 Kaneko, T., & Yokoyama, T. 2017, *ApJ*, 845, 12  
 Karpen, J. T., & Antiochos, S. K. 2008, *ApJ*, 676, 658  
 Karpen, J. T., Antiochos, S. K., Hohensee, M., et al. 2001, *ApJL*, 553, L85  
 Keppens, R., & Xia, C. 2014, *ApJ*, 789, 22  
 Kippenhahn, R., & Schlüter, A. 1957, *ZAp*, 43, 36  
 Kosugi, T., Matsuzaki, K., Sakao, T., et al. 2007, *SoPh*, 243, 3  
 Kuperus, M., & Raadu, M. A. 1974, *A&A*, 31, 189  
 Lemen, J. R., Title, A. M., Akin, D. J., et al. 2012, *SoPh*, 275, 17  
 Leroy, J. L. 1989, *Dynamics and Structure of Quiescent Solar Prominences*, Vol. 150 (Dordrecht: Kluwer Academic), 77  
 Li, D., Ning, Z. J., & Zhang, Q. M. 2015, *ApJ*, 813, 59  
 Li, L., Peter, H., Chitta, L. P., et al. 2021, *ApJ*, 910, 82  
 Li, L., Zhang, J., Peter, H., et al. 2018, *ApJL*, 864, L4  
 Li, Y., & Ding, M. D. 2011, *ApJ*, 727, 98  
 Lites, B. W., Kubo, M., Berger, T., et al. 2010, *ApJ*, 718, 474  
 Liu, C., Deng, N., Lee, J., et al. 2013, *ApJL*, 778, L36  
 Liu, R., Chen, J., Wang, Y., et al. 2016, *NatSR*, 6, 34021  
 Liu, W., Berger, T. E., & Low, B. C. 2012, *ApJL*, 745, L21  
 Liu, Y., Kurokawa, H., & Shibata, K. 2005, *ApJL*, 631, L93  
 Liu, Z., Xu, J., Gu, B.-Z., et al. 2014, *RAA*, 14, 705  
 Luna, M., Karpen, J. T., & DeVore, C. R. 2012, *ApJ*, 746, 30  
 Mackay, D. H., Karpen, J. T., Ballester, J. L., et al. 2010, *SSRv*, 151, 333  
 Martens, P. C., & Zwaan, C. 2001, *ApJ*, 558, 872  
 Martin, S. F. 1998, *SoPh*, 182, 107  
 Mason, E. I., Antiochos, S. K., & Viall, N. M. 2019, *ApJL*, 874, L33  
 Milligan, R. O., & Dennis, B. R. 2009, *ApJ*, 699, 968  
 Moore, R. L., Sterling, A. C., Hudson, H. S., et al. 2001, *ApJ*, 552, 833  
 Neupert, W. M. 1968, *ApJL*, 153, L59  
 Ning, Z., Cao, W., Huang, J., et al. 2009, *ApJ*, 699, 15  
 Okamoto, T. J., Tsuneta, S., Lites, B. W., et al. 2008, *ApJL*, 673, L215  
 Orozco Suárez, D., Asensio Ramos, A., & Trujillo Bueno, J. 2014, *A&A*, 566, A46  
 Parker, E. N. 1953, *ApJ*, 117, 431  
 Pesnell, W. D., Thompson, B. J., & Chamberlin, P. C. 2012, *SoPh*, 275, 3  
 Priest, E. R., & Forbes, T. G. 2002, *A&ARv*, 10, 313  
 Rust, D. M., & Kumar, A. 1994, *SoPh*, 155, 69  
 Schmieder, B., Tian, H., Kucera, T., et al. 2014, *A&A*, 569, A85  
 Schou, J., Scherrer, P. H., Bush, R. I., et al. 2012, *SoPh*, 275, 229  
 Schuck, P. W. 2008, *ApJ*, 683, 1134  
 Shen, Y., Qu, Z., Yuan, D., et al. 2019, *ApJ*, 883, 104  
 Song, H. Q., Chen, Y., Li, B., et al. 2017, *ApJL*, 836, L11  
 Tian, H., Young, P. R., Reeves, K. K., et al. 2015, *ApJ*, 811, 139  
 van Ballegoijen, A. A., & Martens, P. C. H. 1989, *ApJ*, 343, 971  
 Viall, N. M., Kucera, T. A., & Karpen, J. T. 2020, *ApJ*, 905, 15  
 Wang, J., Yan, X., Qu, Z., et al. 2018, *ApJ*, 863, 180  
 Wang, J., Zhang, Y., Zhou, G., et al. 2007, *SoPh*, 244, 75  
 Wang, Y.-M. 1999, *ApJL*, 520, L71  
 Wei, H., Huang, Z., Hou, Z., et al. 2020, *MNRAS*, 498, L104  
 Xia, C., Chen, P. F., Keppens, R., et al. 2011, *ApJ*, 737, 27  
 Xia, C., & Keppens, R. 2016, *ApJ*, 823, 22  
 Xu, Z., Lagg, A., Solanki, S., et al. 2012, *ApJ*, 749, 138  
 Yan, X. L., Jiang, C. W., Xue, Z. K., et al. 2017, *ApJ*, 845, 18  
 Yan, X. L., Priest, E. R., Guo, Q. L., et al. 2016, *ApJ*, 832, 23  
 Yang, B., & Chen, H. 2019, *ApJ*, 874, 96  
 Yang, B., Jiang, Y., Yang, J., et al. 2015, *ApJ*, 803, 86  
 Yang, B., Jiang, Y., Yang, J., et al. 2016, *ApJ*, 816, 41  
 Yang, B., Yang, J., Bi, Y., et al. 2018, *ApJ*, 861, 135  
 Yang, B., Yang, J., Bi, Y., et al. 2019, *ApJ*, 887, 220  
 Young, P. R., Doschek, G. A., Warren, H. P., et al. 2013, *ApJ*, 766, 127  
 Zhang, Q. M., Li, D., Ning, Z. J., et al. 2016, *ApJ*, 827, 27  
 Zhao, X., Xia, C., Keppens, R., et al. 2017, *ApJ*, 841, 106  
 Zhou, Y. H., Chen, P. F., Hong, J., et al. 2020, *NatAs*, 4, 994